Oceanic Density/Pressure Gradients and Slope Currents

JOHN M. HUTHNANCE

National Oceanography Centre, Liverpool, United Kingdom

MARK E. INALL AND NEIL J. FRASER

Scottish Association for Marine Science, Oban, United Kingdom

ABSTRACT

Eastern boundary currents are some of the most energetic features of the global ocean, contributing significantly to meridional mass, heat, and salt transports. We take a new look at the form of an oceanic slope current in equilibrium with oceanic density gradients. We depth integrate the linearized x and y momentum and continuity equations and assume an equilibrium force balance in the along-slope direction (no along-slope variation in the along-slope flow) and zero cross-slope flow at a coastal boundary. We relate the bottom stress to a bottom velocity via a simple boundary friction law (the precise details are easily modified) and then derive an expression for the slope current velocity by integrating upward including thermal wind shear. This provides an expression for the slope current as a function of depth and of cross-slope coordinate, dependent on the oceanic density field and surface and bottom stresses. This new expression for the slope current allows for more general forms of oceanic density fields than have been treated previously. Wind stress is also now considered. The emphasis here is on understanding the simplified equilibrium force balance rather than the evolution toward that balance. There is a direct relationship between the slope current strength, friction, and along-slope forcing (e.g., wind), and also between the total along-slope forcing and bottom Ekman transport, illustrating that "slippery" bottom boundaries in literature are a direct consequence of unrealistically assuming zero along-slope pressure gradient. We demonstrate the utility of the new expression by comparison with a high-resolution hydrodynamic numerical model.

1. Introduction

Eastern (often poleward) boundary currents are common in the oceans, occurring (for example) off Iberia (most obviously in winter; e.g., Frouin et al. 1990), around the United Kingdom (the European Slope Current, e.g., Huthnance 1986; Marsh et al. 2017), off the western United States (California Undercurrent; e.g., Connolly et al. 2014), and off western Australia (the Leeuwin Current; e.g., Smith et al. 1991). They may be seasonal according to the forcing, and obscured at times by wind-driven surface flows, notably in upwelling regions (e.g., Iberia, California). Nevertheless, they may be important contributors to ocean circulation, for example, the European Slope Current contributes about a quarter of

Atlantic inflow to the Nordic seas (Holliday et al. 2015; Lozier et al. 2019) and represents a significant portion of the upper limb of the Atlantic meridional overturning circulation (AMOC).

The oceanic density field with associated pressure gradients has been identified as an important factor of the European Slope Current (Huthnance 1986) and for the Leeuwin Current (Smith et al. 1991). This joint effect of baroclinicity and relief (JEBAR) mechanism reflects the absence of any rest state when an along-slope oceanic density gradient occurs over slope topography. Huthnance (1984) analyzed the poleward development and equilibrium form of the resulting slope current. Along-slope development is also discussed by Csanady (1978). However, the density field in Huthnance (1984) was mainly and severely restricted to be a function only of the along-slope coordinate. Here we consider the equilibrium form, now with more general fields of oceanic density, and with the addition of wind stress. Explicit formulas for the flow field are obtained, so providing scope for
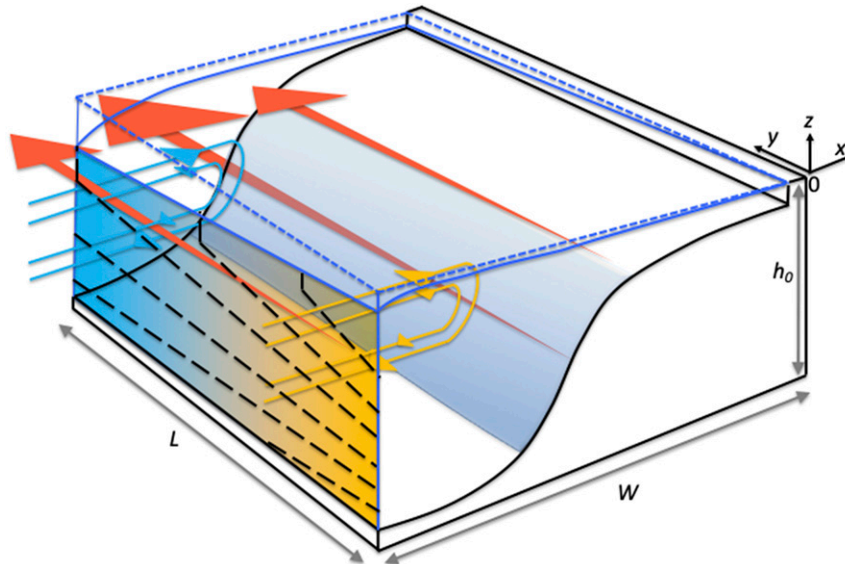
Corresponding author: Mark E. Inall, mark.inall@sams.ac.uk

FIG. 1. Schematic of section 3a scenario, viewed from the southwest. The geostrophically balanced zonal flow is returned in a bottom Ekman layer under the slope current. Yellow to blue shading represents the meridional density gradient (cooler water to the north), Yellow and blue arrows represent both the interior geostrophically balanced zonal flow (horizontal arrow sections) and Ekman flow on the sloping boundary (downslope flow). Red arrows indicate the slope current, intensified over midslope. Perturbation pressure surfaces in the deep ocean are in dashed black lines and planar ocean surface in solid blue lines. Dashed blue lines represent the geoid.

wider-ranging comparison with (and diagnosis or tests of) numerical models in this context where necessary spatial resolution is challenging. We also show that there is a direct relationship between along-slope forcing (arising from a pressure gradient associated with the oceanic density field, or directly from wind stress) and the bottom stress and associated bottom Ekman transport.

2. Analysis

Consider an oceanic margin with depth profile $h(x)$ that is uniform in the alongshore direction y and bounded by a straight coast at $x = 0$ (Fig. 1). Initially assume an oceanic density field $\rho(x, y, z)$, hydrostatic pressure $p = g \int_z^\eta \rho(x, y, z') \, dz'$, below the free surface $z = \eta(x, y)$. Here z is the vertical coordinate and z' a bound (vertical) variable that disappears upon depth integration between definite limits. Then the momentum and continuity equations for velocity (u, v, w) are

$$\rho \left(\frac{\partial u}{\partial t} - fv \right) - \frac{\partial \tau^x}{\partial z} = -\frac{\partial p}{\partial x} = -g\rho_s \frac{\partial \eta}{\partial x} - g \int_z^\eta \frac{\partial \rho}{\partial x} dz', \quad (1a)$$

$$\rho \left(\frac{\partial v}{\partial t} + fu \right) - \frac{\partial \tau^y}{\partial z} = -\frac{\partial p}{\partial y} = -g\rho_s \frac{\partial \eta}{\partial y} - g \int_z^\eta \frac{\partial \rho}{\partial y} dz', \quad (1b)$$

$$\frac{\partial u}{\partial x} + \frac{\partial v}{\partial y} + \frac{\partial w}{\partial z} = 0, \quad (2)$$

where the absent nonlinear advection and lateral viscosity terms are discussed in appendixes A and B. The effects of lateral viscosity (e.g., through eddy action) are, however, implemented in the hydrodynamic model comparison of section 3e (through a variable lateral smoothing length scale). The Coriolis parameter is f, assumed uniform (see appendix C for justification); (τ^x, τ^y) are internal (turbulent) stresses equating to wind stress at the surface and friction at the bottom; and subscripts s and b denote surface and bottom values.

We are considering the simplified equilibrium force balance for along-slope flow, rather than the evolution toward that balance (either in time or along the slope). Hence, we assume $\partial v / \partial y = 0$ for the equilibrated along-slope flow. Depth integrating the continuity Eq. (2) gives

$$\int_{-h}^\eta \frac{\partial u}{\partial x} dz + \int_{-h}^\eta \frac{\partial w}{\partial z} dz = 0,$$

$$\frac{\partial}{\partial x} \left(\int_{-h}^\eta u \, dz \right) - u_s \frac{\partial \eta}{\partial x} - u_b \frac{\partial h}{\partial x} + w_s - w_b = 0,$$

in which the x derivatives arise from the x dependence of the integration limits (h and η). Then the surface and

bottom boundary conditions $w_s = u_s(\partial\eta/\partial x)$ and $w_b = -u_b(\partial h/\partial x)$ imply

$$\frac{\partial}{\partial x}\left(\int_{-h}^{\eta} u\, dz\right) = 0.$$

This states that zonal transport is constant in x, and since there is no flow through the coast at $x = 0$, we must have zero depth-integrated zonal flow everywhere, that is,

$$\int_{-h}^{\eta} u\, dz = 0. \tag{3}$$

Depth integrating the along-slope momentum equation (1) in the steady state $\partial v/\partial t = 0$, neglecting η/h in the final term, neglecting variations of ρ relative to a typical density ρ_s, and using (3), gives

$$0 = \rho_r f \int_{-h}^{\eta} u\, dz = -gh\rho_s\frac{\partial\eta}{\partial y} - g\int_{-h}^{0}\int_{z}^{0}\frac{\partial\rho}{\partial y}\, dz'\, dz + \tau_s^y - \tau_b^y, \tag{4}$$

where τ_s^y, τ_b^y denote along-slope components of surface and bottom stress, respectively. The first term on the RHS of (4) represents the meridional barotropic pressure gradient, the second term the depth-varying meridional pressure gradient, the third term wind stress forcing and the fourth term a retarding bottom stress. Under our assumption of a steady, equilibrated state, surface and bottom stresses may be functions of x but not of y. The form of (frictional) bottom stress τ_b^y is not important except that it should tend to zero for small v_b, for example as for linear or quadratic forms of bed stress $\tau_b^y = r\rho_s v_b$ or $\tau_b^y = C_d|u|v_b$. For simplicity we take the linear form $\tau_b^y = r\rho_s v_b$, with r a linear bottom friction coefficient, with units of meters per second (m s^{-1}).

In the deep ocean (with depth h_0 and surface stress τ_{s0}^y) we assume that the (meridional) bottom current is small, and therefore neglect τ_b^y. In other words, the underlying premise in depth integrating (1b) to give the oceanic meridional (along slope) pressure gradient [i.e., the surface slope in (4) in the deep ocean, away from the slope], is that the overall deep-ocean meridional (alongshore) flow is weak, and τ_b^y therefore negligible. This is justified, for example, 0.01 m s^{-1} in 2-km depth and 5000-km breadth corresponds to 100 Sv (1 Sv $= 10^6$ m^3 s^{-1}), which is much greater than the alongshore (typically meridional) transport integrated over any ocean basin.

Hence from (4)

$$\frac{\partial\eta}{\partial y} = -\frac{1}{(h_0\rho_s)}\left(\int_{-h_0}^{0}\int_{z}^{0}\frac{\partial\rho}{\partial y}\Big|_{x=-W}\, dz'\, dz + \frac{\tau_{s0}^y}{g}\right), \tag{5}$$

where $x = -W$ is the oceanward edge of the base of the continental slope, with W being the width of the ocean margin (as in Fig. 1); all terms in (5) are evaluated at $x = -W$.

Now we again invoke the simplified equilibrium force balance so that terms in (1a), in particular $\partial\eta/\partial x$, are independent of y. Hence $(\partial^2\eta/\partial x\partial y) = (\partial^2\eta/\partial y\partial x) = 0$, that is, the zonal sea surface gradient may not vary meridionally, and vice versa; but note that $\partial^2\eta/\partial x^2$ is not necessarily zero, allowing for curvature of the sea surface height field in the x direction (depicted schematically in Fig. 1). On the sloping margin from (4) and after substituting for $\partial\eta/\partial y$ from (5) and for $\tau_b^y = r\rho_s v_b$,

$$r\rho_s v_b = g\frac{h}{h_0}\int_{-h_0}^{0}\int_{z}^{0}\frac{\partial\rho}{\partial y}\Big|_{x=-W}\, dz'\, dz$$
$$- g\int_{-h}^{0}\int_{z}^{0}\frac{\partial\rho}{\partial y}\, dz'\, dz - \frac{h}{h_0}\tau_{s0}^y + \tau_s^y. \tag{6}$$

For example, if there is no surface (wind) stress and density ρ is a function of y only (with no x or z variation), then as in Huthnance (1984, section 5b)

$$v(x) = v_b = \frac{gh(h_0 - h)}{2\rho_s r}\frac{\partial\rho}{\partial y}. \tag{7}$$

However, (6) allows for more general density fields and for wind forcing, unlike the expression in Huthnance (1984). The main constraint in this new derivation is the assumption of zero along-slope divergence, that is, that $\partial v/\partial y = 0$; that is to say, the along-slope flow has reached equilibrium with the wind forcing and pressure field and is not evolving along the slope. The term v_b is given by (6), and by integrating the thermal wind relation $f(\partial v/\partial z) = -(g/\rho_s)(\partial\rho/\partial x)$ in the cross-slope momentum equation (1a) vertically from the seabed we obtain the z dependence implied by geostrophic balance

$$v = v_b - \frac{g}{f\rho_s}\int_{-h}^{z}\frac{\partial\rho}{\partial x}\, dz'. \tag{8}$$

Hence $\partial v/\partial y = 0$ is satisfied if both RH terms of (8) are independent of y.

First therefore, we require $\partial v_b/\partial y = 0$, which is satisfied if $(\partial^2\rho/\partial y^2) = 0$ by (6). Thus $\partial\rho/\partial y$ may be a function of x and z only (not y). We now define ρ_y accordingly, $\rho_y(x, z) = \partial\rho/\partial y$. Integrating this expression again with respect to y similarly yields $\rho = \rho_y(x, z)y + \rho_2(x, z)$, and in so doing defines the constant of integration ρ_2 as the density field as a function of x and z, at some arbitrary location $y = 0$.

Second, we require the last term of (8) to be independent of y. This is true if $\partial^2\rho/\partial x\partial y = 0$ so that ρ_y is independent of x, that is,

$$\rho = \rho_y(z)y + \rho_2(x, z). \quad (9)$$

We note that (9) and its antecedents may not be necessary conditions for zero along-slope divergence since (6) and (7) only impose integral constraints on $\partial^2\rho/\partial y^2$ and $\partial^2\rho/\partial x\partial y$. However, (9) is a sufficient condition. [With this notation $\partial\rho/\partial y = \rho_y(z)$.]

Given (9), v_b is given by (6) with ρ_y in place of $\partial\rho/\partial y$ and $v(x, z)$ by (5) with $\partial\rho_2/\partial x$ in place of $\partial\rho/\partial x$ (noting the definition given above of ρ_2 as the density field as a function of x and z, at some arbitrary location $y = 0$). Thus, v, the slope current, is given by (8) as

$$v = \frac{1}{\rho_s r}\left[g\frac{h}{h_0}\int_{-h_0}^{0}\int_{z}^{0}\rho_y(z')\,dz'\,dz - g\int_{-h}^{0}\int_{z}^{0}\rho_y(z')\,dz'\,dz \right.$$
$$\left. - \frac{h}{h_0}\tau_{s0}^y + \tau_s^y \right] - \frac{g}{f\rho_s}\int_{-h}^{z}\frac{\partial\rho_2}{\partial x}\,dz', \quad (10)$$

with two separate, additive component parts for ρ, given by (9), comprising the y-dependent component $\rho_y(z)y$, and x-dependent component $\rho_2(x, z)$. On the RHS of (10), the two double integral terms in ρ_y represent what has been called JEBAR forcing of the slope current. Explicitly, this is the difference between the depth-integrated pressure gradient evaluated at the x location in question, and that evaluated at the deep ocean boundary and scaled by relative water depth $h(x)/h_0$. It expresses that the deep-ocean force balance, with the y gradient of pressure through the full oceanic depth, implies an imbalance (offset by bottom friction) on the shelf and slope that only experience the upper part of the meridional pressure gradient field, as detailed in section 3a. The next two terms are due to wind stress forcing. Vertical (z) dependence of this solution comes only through the last term in (10), which derives from the geostrophic balance (8) of z shear with cross-slope density gradient. Cross-slope (x) dependence may come explicitly through the last term in (10), implicitly through the x dependence of depth (h) in all terms, and through x dependence of the surface stress τ_s^y (and, indeed, x dependence in the bottom stress term could be incorporated through r, see the discussion section on why this might be physically reasonable).

For illustrative purposes, we consider a particular example of (10): that is, for uniform ρ_2 and an alongshore density gradient only above a thermocline (depth h_T), that is, $\rho_y = 0$ ($z < -h_T$) and uniform ρ_y in the region $z > -h_T$ (above the thermocline). Then if there is no surface (wind) stress

$$v(x) = v_b = \frac{g\rho_y}{2\rho_s r h_0}[h_T^2(h_0 - h)], \quad h > h_T,$$

or

$$v(x) = v_b = \frac{g\rho_y}{2\rho_s r h_0}h(2h_0 h_T - h_T^2 - h_0 h), \quad h < h_T.$$

3. Discussion

a. Physical description of slope-current forcing

For definiteness, consider the meridional eastern margin of an idealized Northern Hemisphere ocean (Fig. 1). Note that the slope current results from the along-slope component of density gradient; the meridional orientation in this scenario is not necessary. The density of the ocean (at least of an upper layer) decreases toward the equator. Equation (5) determines a meridional oceanic surface slope on the basis of small bottom stress. In the absence of other forcing (in particular, if the wind stress τ_{s0}^y is zero), there is nothing to balance the depth-integrated meridional pressure gradient, which is therefore zero. Thus, the meridional pressure gradient geostrophically balances zero depth-integrated zonal flow at all points toward the coast [as represented by (4); there is no "spare" pressure gradient accelerating meridional flow through the deep ocean]. However, the meridional density gradient implies depth variation of the meridional pressure gradient [the first two terms on the RHS of (1b)]. Near the surface, the surface slope implies a poleward force (pressure decreases poleward). Near the bottom, the meridional gradient of (hydrostatic) pressure is reversed owing to the density gradient and the condition (5) of zero depth integral. A sufficient condition for positive JEBAR term at all values of slope depth, h, is $\rho_y > 0$ for all z. As an illustration of the JEBAR term for the rendition of (10) using the numerical model density field discussed in section 3e, the meridional density and pressure gradient fields are shown as functions of depth and related to the effective JEBAR over varying slope depth at four locations (Fig. 2). The water depth over the slope is less than in the deep ocean. Therefore, the depth integral of the meridional pressure gradient [the first two terms on the RHS of (1b)], on the slope and shelf, omits at least some of the reversed deeper pressure gradient, that is, the depth-integrated pressure gradient acts as a poleward force in the same sense as the surface slope. This is a barotropic force over and along the slope, with the baroclinic component balanced by the vertical shear of the zonal cross-slope flow [represented by the z derivatives of the (1b) terms in u and $\partial\rho/\partial y$]. In the steady state, this meridional barotropic force is balanced by bottom frictional stress [represented by τ_b^y in (4)] on an along-slope flow, leading to (6) [and hence (10)] if $\tau_b^y = r\rho_s v_b$.
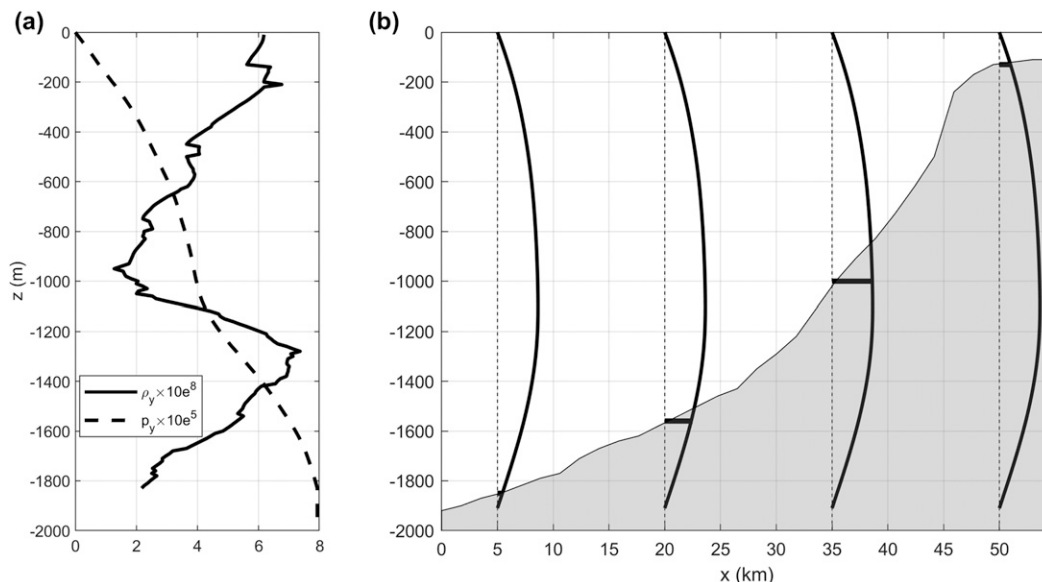
FIG. 2. (a) $\partial\rho/\partial y(z)$ plotted alongside its depth integral [i.e., the "inner" integral present both in terms 1 and 2 of (10)], which represents the meridional baroclinic pressure gradient. As this inner integral is monotonically increasing, its depth integral (term 2 where h is the depth coordinate) is curved in z such that it is smaller than a straight line between its end points (term 1) for all values of z. (b) JEBAR (term 1 + term 2) is depicted as a function of z at the four different slope depths: near the ocean boundary, two on midslope, and on the shelf. Although this is a barotopic term, its value is derived from the values of the depicted curve where it intersects the slope. JEBAR is therefore zero at the ocean boundary and small on the shelf, but maximal over the sloping margin.

If the along-slope flow is "too weak," physically it is accelerated by the "excess" pressure gradient minus the effects of frictional stress until a new balance is reached with a faster along-slope flow.

Over the slope, the depth is less than oceanic; the deeper oceanward flow is missing from the geostrophically balanced zonal cross-slope flow. However, it is contained in the Ekman transport (Fig. 1) associated with the meridional bottom stress that balances the depth-integrated meridional pressure gradient.

b. Forcing, stress, and Ekman transport

Equation (4) shows a very direct relation between the bottom stress (on the one hand) and (on the other hand) the combined along-slope components of surface (wind) stress and pressure gradient (here the result of a surface slope and along-slope density gradient). Although along-slope uniformity of the flow is assumed, it is clear that the bottom stress (related to current strength) is determined directly by the forcing arising from the pressure gradient. The bottom stress should not be "defined away" by an assumption of zero along-slope wind stress and pressure gradient, which in any case varies with depth. In general bottom stress τ_b is nonzero in (4) and a cross-slope Ekman transport τ_b/f results.

c. The density field

The density components $\rho_y(z)y$ and $\rho_2(x, z)$ in (9) allow for stratification and indeed for depth variation of the along-slope flow through (8). However, stratification may affect the bottom Ekman layer. Assuming stable stratification, an Ekman layer with downslope transport reduces stratification and is thicker than an Ekman layer with upslope transport, which intensifies stratification and is thereby inhibited (Brink 2016). These considerations have been neglected here, another idealisation along with the alongshore uniformity and steady state that constrain the density field. Diffusion in the cross-slope plane tends to reduce these effects of stratification.

In principle (Huthnance 1984) the velocity evolves along the slope (and in time) toward the equilibrated form. Coastal-trapped waves carry the information about initial conditions and hence the evolution space and time scales are expected to be set by their decay distance and time. Typically these scales will be of the order of hundreds of kilometers and days, but depend strongly on the context and the forcing pattern. If the forcing matches higher-mode coastal-trapped waves, the scales will be shorter, as also with strong friction or a narrow shelf with weak stratification. Density fields approximating the form (9) over an extent greater than

the evolution space and time scales may be expected to give near-equilibrated velocity approximating (10). Oceanic eddies impinging on the slope, and storms, are likely to cause departure from (10) owing to short spatial and time scales, respectively.

Variations in slope topography are subject to similar considerations. However, the main impact of changes in slope steepness is to accelerate or retard the primarily geostrophic flow to maintain along-slope transport between any pair of converging or diverging isobaths. Such adjustment can take place on shorter scales (typically tens of kilometers).

d. Representing a realistic density field

Evolution of the velocity along the slope (discussed in section 3e) is forced by mismatch between its form at any one location and the equilibrium form implied by density gradients. The mismatch has components from (6) and from (8). Equation (6) relates the strength of the near-bed slope current to the along-slope density gradient; cross-slope dependence is entirely related to water depth if the condition $\partial^2\rho/\partial x\partial y = 0$ is satisfied. Then (8) completes the distribution over the cross-slope section by relating the vertical structure of the current to the cross-slope density gradient $\partial\rho/\partial x$. To represent a realistic density field in the form (9), one must take cross slope density section, $\rho_2(x, z)$, with oceanic boundary sufficiently deep that the approximation of $\tau_b^y = 0$ is valid, and shelf boundary shallow enough that no slope current structure is omitted. For $\rho_y(z)$, one must linearize the along-slope density gradient at each depth level, over a length scale representative of large-scale meridional density gradient [typically $O(100)$ km]. Ideally, given sufficient along-slope data, one should take the linear along-slope density trend. However, this can also be achieved by taking the difference between two near-slope density profiles with appropriate meridional spacing, taking care not to alias smaller-scale density structure local to the profiles (e.g., via spatial or temporal averaging).

Differences between the original and fitted forms of density through this process arise if the density variation along the slope is either nonlinear or varies across the slope. The variance of the differences between the true density and the fitted form (9) can be compared with the variance of the true density to estimate the quality of the fit.

e. Comparison with a numerical model

As a demonstration of how one might apply (10), the procedure in section 3d was applied to the February 2018 density field, 100 km in along-slope extent between the 200- and 1700-m isobaths, from the numerical Atlantic Margin Model, 1.5 km (AMM15; Graham et al. 2018) at 56°N on the Hebrides shelf and

slope west of Scotland. AMM15 is a 1.5-km resolution NEMO configuration, now the U.K. operational forecast model for the northwest European shelf and adjacent Rockall Trough. Figure 3 shows the resulting along-slope velocity field from (10) (with $r = 0.01$ m s^{-1} and $\tau_s = 0.1$ Pa, approximately the mean value for along-slope wind stress from ERA-Interim in our region during February 2018) alongside the corresponding modeled currents. The value of $r = 0.01$ m s^{-1} was chosen such as to give comparable volume transports in (10) and AMM15. The analytical solution was smoothed laterally using a 15-km smoothing window, calculated based upon the analysis in appendix B, to simulate the effect of lateral viscosity.

The two solutions are in general agreement over the vertical structure of the slope current and both show flow reversals at depth over the lower slope and on the shelf. Both solutions show northward bottom currents over the upper slope. Figure 4 shows the depth integrals of the thermal wind, JEBAR, and wind forcing terms (where the second two are anyway barotropic), and demonstrates that this feature is largely a result of JEBAR (with a small contribution from wind stress). There is some disagreement in the horizontal structure, with the diagnosed form (10) (Fig. 3a) giving a narrow and stronger current core around $x = 25$ km. The positive bottom velocities over the upper slope in (10) are weaker than those in the numerical solution. The southward undercurrent over the lower slopes is also slower in the numerical solution. Expressed as integrated volume transports, the three terms equate to JEBAR = 0.6 Sv, wind = 0.14 Sv, and thermal wind = 0.82 Sv. Several mechanisms may account for disagreement between the analytic and numerical solutions:

1) An explanation of the narrower slope current may lie with the application in (10) of a constant linear bottom friction. If, instead, r varies inversely with water depth h (e.g., because tidal currents contributing to linearized bottom stress will be weaker in deep water) then (10) would enhance the slope current in deeper water through the extra proportionality to h, giving rise to a slope current biased farther offshore than seen in Fig. 3a but retaining the same on/offshore extent;

2) A uniform wind stress has more effect in shallower water, but may add or detract from the density-driven slope current according to its direction. The application of a stronger southerly wind stress to (10) would preferentially enhance along-slope flow on the upper slope.

3) On/off-shelf tidal currents in AMM15 may advect the slope current, spreading its cross-slope distribution in the averaged field shown. If we simply assume
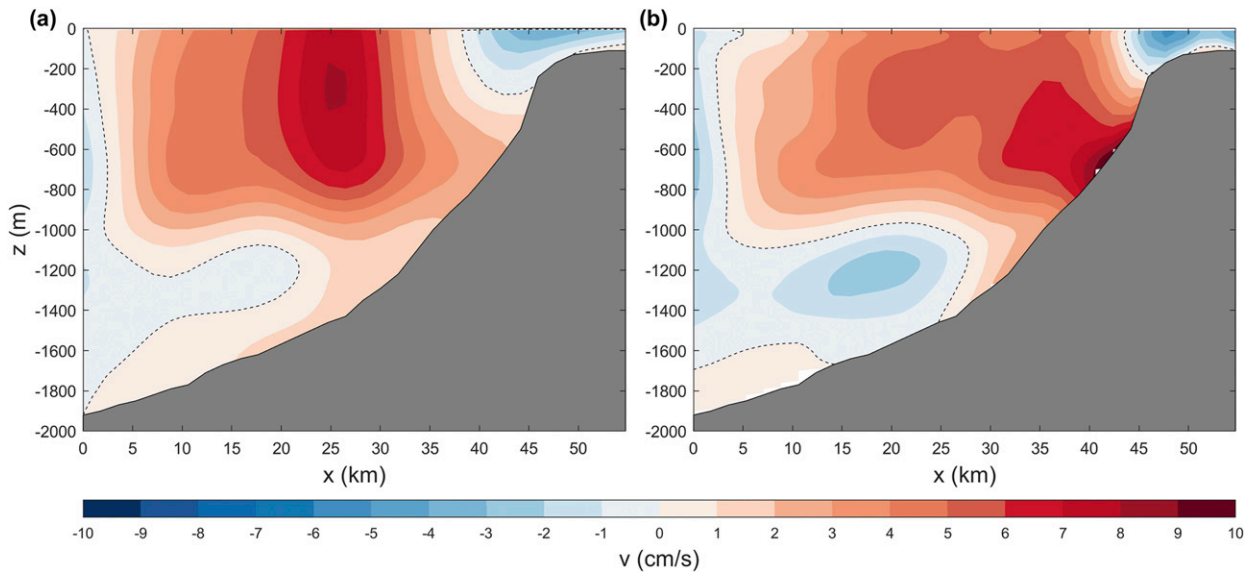
FIG. 3. Comparison of (a) the meridional velocity derived from the AMM15 density field using (10) with (b) the corresponding AMM15 velocity field at a portion of the slope near 56°N west of Scotland. Both fields are averaged spatially, over the along-slope coordinate, and temporally, over February 2018. A spatially uniform along-slope wind stress of 0.1 Pa was imposed for (a), corresponding to ERA-Interim reanalysis values.

that a cross-slope tidal displacement $X(t)$ causes the slope current seen at x to be $v(x - X)$, then the average over a sinusoidal tidal cycle of period T is $T^{-1} \int_0^T v[x - UT(2\pi)^{-1} \cos(2\pi t/T)] \, dt$. For the simplest case (7) with h linear in x, $v(x) = 4Vx(W - x)W^{-2}$; for width W without tidal advection and maximum V. With tidal advection the average becomes $4VW^{-2}[x(W - x) - (U'^2/2)]$ provided $U' < x < W - U'$ (requiring $U' \equiv UT/(2\pi) < W/2$). The reduced maximum is now $V[1 - (2U'^2/W^2)]$ and evidently the slope current is spread by U' to either side. In the context of the comparison with tidal currents of order $0.1 \, \mathrm{m \, s^{-1}}$ and hence displacement amplitudes of order 1 km, the overall slope current of width order 30 km will not be much affected but finer structure associated with $\rho_2(x, z)$ may be smoothed.

4) Tidal rectification is expected to give an added poleward flow over the upper slope (mainly in water of depth $h < 500$ m; Stashchuk et al. 2017). Tides and tidal rectification are included in the AMM15 velocity field (AMM15 contains tides) but tides are beyond the scope of the present analysis. However, tidal rectification may be regarded as additional forcing as discussed in item ii in appendix D. The cross-slope distribution of tidally rectified along-slope flow, as $h^{-3}(\partial h/\partial x)fQ^2\sigma^2$ (item ii in appendix D), is concentrated close to the shelf break combining shallow depth and steep slope. This is typically narrower and further on-shelf compared with a JEBAR-forced slope current such as (7).

Thus, we expect more realistic bottom friction and the addition of tidal effects to broaden the slope current from (10) to a closer comparison with the AMM15 field in Fig. 3. Both these are topics of ongoing investigation.

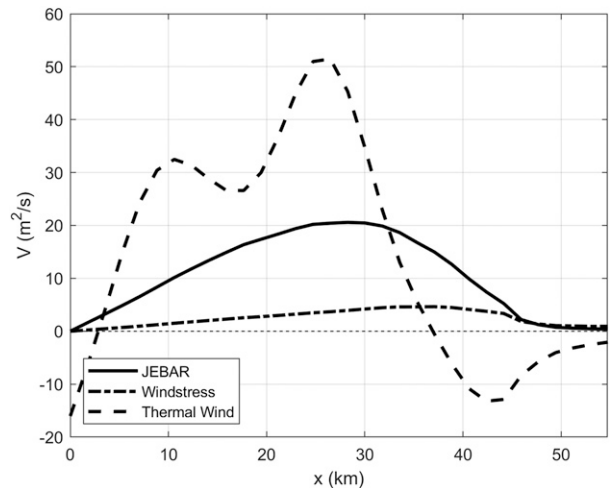Further discrepancies between the time averaged AMM15 velocity field and the steady analytic solution

FIG. 4. Depth-integrated transport associated with JEBAR [terms 1 and 2 in (10)], wind stress (terms 3 and 4), and thermal wind shear (term 5). Only the thermal wind term has z dependence, visualized in Fig. 3. Area integrated (volume) transports equate to JEBAR = 0.6 Sv, wind = 0.14 Sv, and thermal wind = 0.82 Sv. Total volume transport = 1.56 Sv.

evaluated solely using the AMM15 density field may arise from topographical irregularities and unsteadiness in the modeled flow. Within the model density averaging grid, the slope width (between 200 m representing the shelf break, and 1700 m) varies by a factor of about 2. This variation is fairly gradual and is closely followed by along-slope flow. However, ~15 km "upstream" (to the south) is a marked indentation or "canyon" in the slope, mainly showing in the depth range 500–1700 m. The canyon, width $O(10)$ km, is known to affect the cross-slope distribution of internal wave energy at tidal frequencies, locally and to the north, that is, impinging on our grid area (Stashchuk and Vlasenko 2017).

Regarding flow steadiness: Direct current observations over an annual cycle (Souza et al. 2001) reveal steadiness factors between 0.8 and 0.9 in summer, and about 0.7 in winter, and show that (in summer) the ratio of RMS along-slope velocity to the mean in the core of the slope current is less than 0.5. To quantify unsteadiness in the modeled flows we examined 5-day averages of NEMO modeled transport magnitude at 55.7°N between 10° and 8°W from 2010 to 2013 (Guihou et al. 2017; J. Polton 2020, personal communication). This analysis reveals that 77% of the total variance in the 5-day values remains in monthly mean values. Further, almost half the monthly variance is in the seasonal cycle. Thus, while there is modeled flow variability at time scales shorter than our one month averaging window, there remains a greater proportion of the variance (77%) at time scales one might consider to be steady from the point of view of a geostrophic solution, that is, monthly or greater.

We note that NEMO AMM15, in common with other three-dimensional hydrodynamic models, uses a smaller value for r as a linear bottom drag term ($\sim 1 \times 10^{-3}$) than used in our evaluation of (10). In AMM15 there will be rapid communication in the vertical of bottom boundary conditions through the model's vertical viscosity parameterization. To achieve this NEMO uses a global, gridded field of barotropic to baroclinic tidal energy conversion rate (Simmons et al. 2004) and as a result is highly vertically viscous on the northwest European slope, a region of strong internal tide generation (e.g., Inall et al. 2000; Inall et al. 2011). This may be another factor explaining why we need a large value for r to reproduce in the depth-integrated (10) the same transport as seen in AMM15.

A final note is made in reference to the commonly cited heuristic slope current descriptions (e.g., Simpson and Sharples 2012, and references therein). In these descriptions, the zonal sea surface gradient increases with latitude (depicted in cartoon illustrations; e.g.,

Simpson and Sharples 2012, p. 213), and hence in the geostrophically balanced state $\partial v / \partial y > 0$. This is not allowed in the present formulation, but we would argue there is no strong evidence in the literature for European Slope Current transport to increase with latitude.

4. Conclusions

The form of an "equilibrium" slope current has been derived for a wider range of oceanic density fields than in previous literature (Huthnance 1984). There are still constraints by assumptions that forcing and flow are quasi-uniform along the slope.

A direct relationship exists between along-slope forcing (arising from the pressure gradient) and the bottom stress and Ekman transport. This implies that along-slope pressure gradient should not be assumed zero. Indeed the along-slope pressure gradient varies with depth in the presence of along-slope density gradients. It also responds to any forcing [here we took a depth integral (4) to determine $\partial \eta / \partial y$ and hence the along-slope pressure gradient in relation to the forcing].

Boundary currents are energetic features of the global ocean, contributing significantly to meridional mass, heat, and salt transports and yet they are poorly resolved in global hydrodynamic models, sparsely measured by global observing systems, and the literature on the underlying dynamical balances is modest. Our hope is that this note contributes to the latter, and provides a new dynamical framework for further investigation of the roles of bed friction, wind stress, and changing oceanic density fields on the shape and strength of the slope currents of the world's ocean basins.

APPENDIX A

Neglected Terms: Advection

Advection is represented by the hitherto neglected nonlinear terms ($-\rho \mathbf{u} \cdot \nabla u$, $-\rho \mathbf{u} \cdot \nabla v$) in (1). We distinguish between the y–uniform steady flow of (10) and other flows which are in effect additional forcing discussed in appendix D.

Here we evaluate $(-\rho \mathbf{u} \cdot \nabla u, -\rho \mathbf{u} \cdot \nabla v) = \{-\rho[u(\partial u/\partial x) + w(\partial u/\partial z)], -\rho[u(\partial v/\partial x) + w(\partial v/\partial z)]\}$ on the basis of (10).

An explicit expression for cross-slope u follows from the steady form of (1b) using (5) for $\partial\eta/\partial y$ and then (9):

$$\rho f u = \frac{\partial\tau^y}{\partial z} + \frac{g}{h_0}\left(\int_{-h_0}^{0}\int_{z}^{0}\rho_y(z')\,dz'\,dz + \frac{\tau_{s0}^y}{g}\right)$$
$$- g\int_{z}^{0}\rho_y(z')\,dz'.$$

For *density gradients only (no wind stress)*, $\partial u/\partial x = 0$ in the interior and, in the simplest case of $\partial\rho_y/\partial z = 0$ leading to (7),

$$-\rho u\frac{\partial v}{\partial x} = -g^2\rho_y^2\frac{\partial h}{\partial x}(h_0 - 2h)\left(\frac{h_0}{2} + z\right)\frac{1}{2f\rho_s r}.$$

Moreover, in this simplest case w is of order $u(\partial h/\partial x)$, $\rho f(\partial u/\partial z) = (\partial^2\tau^y/\partial z^2) + g\rho_y$, $\partial v/\partial z = 0$.

Thus the expressions for $-\rho u(\partial v/\partial x)$ and $-\rho w(\partial u/\partial z)$ [i.e., its scaling $(u/f)(\partial h/\partial x)g\rho_y$] are to be compared with the other terms in (1b), for example the bottom stress distributed through the water column:

$$\tau_b^y/h = \frac{r\rho_s v_b}{h} = \frac{g(h_0 - h)\rho_y}{2}$$

by (7). The ratios are of order $\rho_y(\partial h/\partial x)h_0 g/(2f\rho_s r)$, $g\rho_y(\partial h/\partial x)/(\rho f^2)$, respectively, and represent conditions

that the JEBAR term $\rho_y(\partial h/\partial x)g/(2f\rho_s)$ is not too large (relative to the bottom stress r/h_0 in the first case). For example, if (as in Huthnance 1984) $\rho_y h_0/\rho_s = 10^{-7}$, $g = 10\,\mathrm{m\,s^{-2}}$, $f = 10^{-4}\,\mathrm{s^{-1}}$, $r/h_0 = 10^{-6}\,\mathrm{s^{-1}}$, $\partial h/\partial x = h_0/(100\,\mathrm{km}) = 10^{-2}$ then the ratios are 0.05 and 0.001, respectively, and indeed small. The conditions may be broken if friction is relatively weak or the JEBAR factor $\rho_y(\partial h/\partial x)$ is relatively strong.

For only wind stress forcing,

$$\rho f u = \frac{\partial\tau^y}{\partial z} + \frac{\tau_{s0}^y}{h_0},$$

$$\rho f\frac{\partial u}{\partial x} = \frac{\partial^2\tau^y}{\partial x\partial z},$$

$$\rho f\frac{\partial u}{\partial z} = \frac{\partial^2\tau^y}{\partial z^2},$$

$$v = \frac{1}{\rho_s r}\left(\tau_s^y - \frac{h}{h_0}\tau_{s0}^y\right),$$

$$\frac{\partial v}{\partial x} = \frac{1}{\rho_s r}\left[\frac{\partial\tau_s^y}{\partial x} - \frac{\partial h}{\partial x}\frac{\tau_{s0}^y}{h_0}\right], \quad\text{and}$$

$$\frac{\partial v}{\partial z} = 0,$$

leading to advection terms

$$(-\rho\mathbf{u}\cdot\nabla u, -\rho\mathbf{u}\cdot\nabla v) = \left[-\rho\left(u\frac{\partial u}{\partial x} + w\frac{\partial u}{\partial z}\right), -\rho\left(u\frac{\partial v}{\partial x} + w\frac{\partial v}{\partial z}\right)\right]$$
$$= \left[-\frac{1}{\rho f^2}\left(\frac{\partial\tau^y}{\partial z} + \frac{\tau_{s0}^y}{h_0}\right)\frac{\partial^2\tau^y}{\partial x\partial z} \quad\text{and order}\quad \frac{1}{\rho f^2}\left(\frac{\partial\tau^y}{\partial z} + \frac{\tau_{s0}^y}{h_0}\right)\frac{\partial h}{\partial x}\frac{\partial^2\tau^y}{\partial z^2},\right.$$
$$\left.-\frac{1}{\rho_s r f}\left(\frac{\partial\tau^y}{\partial z} + \frac{\tau_{s0}^y}{h_0}\right)\left(\frac{\partial\tau_s^y}{\partial x} - \frac{\partial h}{\partial x}\frac{\tau_{s0}^y}{h_0}\right)\right].$$

In comparison with the (1a) and (1b) terms $(-\rho f v, \partial\tau^y/\partial z$ or $\tau_b^y/h = r\rho_s v_b/h)$ and for simplicity taking a localized wind stress so that $\tau_{s0}^y = 0$, the respective ratios are of order

$$\left(\frac{\tau_s^y}{\rho f}\frac{r}{hLhf^2}\quad\text{and}\quad \frac{\tau_s^y}{\rho f}\frac{r}{hLhf^2}, \frac{\tau_s^y}{\rho frL}\right),$$

where L is an on/offshore scale for variation of the wind stress [in the case of $u(\partial u/\partial x)$] or depth [in the case of $w(\partial u/\partial z)$]. For example, if the wind stress is such as to give an Ekman transport $\tau_s^y/\rho f = 1\,\mathrm{m^2\,s^{-1}}$, $L = 100\,\mathrm{km}$, $f = 10^{-4}\,\mathrm{s^{-1}}$, $r/h_0 = 10^{-6}\,\mathrm{s^{-1}}$ as before with $h = h_0 = 1\,\mathrm{km}$ then the ratios are of order $(10^{-6}, 10^{-2})$. The condition is not so well satisfied if winds are very strong (large τ_s^y) and localized (small L).

APPENDIX B

Neglected Terms: Lateral Viscosity

Lateral viscosity is neglected in our analysis but present in the comparator numerical model. Its expected general effect is to broaden any forced flow. We illustrate this effect most simply with flow of uniform density in uniform depth along the ocean margin (i.e., in direction y) under forcing localized in x and derive a diffusive length scale L as follows.

The RHS of (1b) has an additional viscous term $\mu(\partial^2 v/\partial x^2)$. Hence for flow of uniform density in uniform depth along the ocean margin (i.e., in direction y) under forcing localized in x, (4) becomes

$$0 = gh\rho_s \frac{\partial \eta}{\partial y} + \tau_s^y - \tau_b^y + \left(\int_{-h}^{0} \mu \frac{\partial^2 v}{\partial x^2} dz = \mu \frac{\partial^2}{\partial x^2} \int_{-h}^{0} v\, dz \right).$$

Assuming that $v \to 0$ in the ocean far from the coast and localized forcing, (5) becomes

$$gh\rho_s \frac{\partial \eta}{\partial y} = -\tau_{s0}^y = 0.$$

Eliminating $h\rho_s(\partial\eta/\partial x)$, writing $\tau_b^y = r\rho_s v_b$ as before and simplifying v_b as $\alpha V/h$, $V \equiv \int_{-h}^{0} v\, dz$, α being a factor $O(1)$ to allow for $v_b \neq V/h$, we have

$$r\rho_s \frac{\alpha V}{h} - \mu \frac{\partial^2 V}{\partial x^2} = \tau_s^y.$$

This gives exponential decay away from localized forcing on a decay/diffusive length scale $L \equiv (\mu h/r\rho\alpha)^{1/2}$. For example, if $r/h_0 = 10^{-6}\,\mathrm{s}^{-1}$, $\mu/\rho = 100\,\mathrm{m^2\,s^{-1}}$, and $\alpha = 1$, then $L = 10\,\mathrm{km}$. We show an example with JEBAR form $gh(h_0 - h)\rho_y/2$ [see (6) and (7)] with h replaced by $-Sx$ (where S is the implicit slope that defines the width of forcing); this forcing applies in $-h_0/S < x < 0$ and is zero elsewhere in x. Thus

$$L^{-2}V - \frac{\partial^2 V}{\partial x^2} = -g'x(h_0 + Sx); \quad g' \equiv \frac{gS\rho_y}{2\mu h_0},$$

with solution

$$V = V_F e^{x/L} \quad \left(-\infty < x < -\frac{h_0}{S} \right);$$

$$V = -(2SL^2 + h_0 x + Sx^2)g'L^2 + V_+ e^{x/L}$$
$$+ V_- e^{-x/L} \quad \left(-\frac{h_0}{S} < x < 0 \right);$$

$$V = V_C \sinh\left(\frac{x - X}{L} \right) \quad (0 < x < X),$$

where the term in g' is a particular integral matching the forcing; the exponentials are solutions of the unforced equation with coefficients chosen to satisfy boundary conditions $V \to 0$ as $x \to -\infty$, V and $\partial V/\partial x$ are continuous at $x = -h_0/S$ and $x = 0$, and $V = 0$ at the coast $x = X$. Hence,

$$V_C = g'L^3[2LS - h_0 - (2LS + h_0)e^{-h_0/(SL)}]e^{-X/L},$$

$$V_+ = \frac{g'L^3}{2}\{2LS + h_0 + [2LS - h_0 - (2LS + h_0)e^{-h_0/(SL)}] \\ \times e^{-2X/L}\},$$

$$V_- = \frac{g'L^3}{2}(2LS + h_0)e^{-h_0/(SL)}, \quad \text{and}$$

$$V_F = \frac{g'L^3}{2}\{(h_0 - 2LS)e^{h_0/(SL)} + 2LS + h_0 \\ + [2LS - h_0 - (2LS + h_0)e^{-h_0/(SL)}]e^{-2X/L}\}.$$

For large X (coast distant from forcing) we isolate the effect of lateral viscosity. Then $e^{-2X/L} \to 0$ and in $-h_0/S < x < 0$

$$V/(g'L^2) = -(2SL^2 + h_0 x + Sx^2) + L(2LS + h_0) \\ \times \cosh\left\{ \frac{[x + h_0/(2S)]}{L} \right\} e^{-h_0/(2SL)}.$$

In comparison with zero lateral viscosity, this remains symmetric about the location $x = -h_0/(2S)$ of maximum forcing, but the value of V there is

$$V = \frac{gSh\rho_y}{2r\alpha\rho h_0}[-2SL^2 + h_0^2/4S + L(2LS + h_0)e^{-h_0/(2SL)}],$$

and

$$V = \frac{gSh\rho_y}{2r\alpha\rho h_0}[-2SL^2 + L(2LS + h_0)(1 + e^{-h_0/SL})/2]$$

at $x = -h_0/S$ or 0. Writing $a \equiv h_0/2SL$ and omitting a common factor $gh\rho_y h_0/2r\alpha\rho$, these values are plotted for $0 \leq a \leq 5$ (Fig. B1) corresponding to decreasing lateral viscosity (diffusive length scale L relative to half-width $h_0/2S$ of forcing) as a increases. For small lateral viscosity, the maximum flow at $x = -h_0/2S$ tends to its value without lateral viscosity and to zero outside the range of forcing. As lateral viscosity increases, the maximum flow decreases (e.g., to less than half its no-lateral-viscosity value for $L = h_0/2S$) and the relative magnitude at the edges of the forcing increases.

APPENDIX C

Neglected Terms: Spatial Variation in f

Spatial (along slope) variation of Coriolis parameter f is considered by Furue et al. (2013) in the context of the Leeuwin Current but with more general applicability. In the region where the flow experiences the sloping bottom, their solution is propagated poleward along f/h contours and hence off shelf as f increases in magnitude. This finding is supported by numerical calculations in Benthuysen et al. (2014). The assumption of uniform f in the present analysis corresponds to supposing that flow evolves to the equilibrium form (sought here) "faster" than f/h evolves along the shelf ("faster" being in the sense of short along-shelf distance).
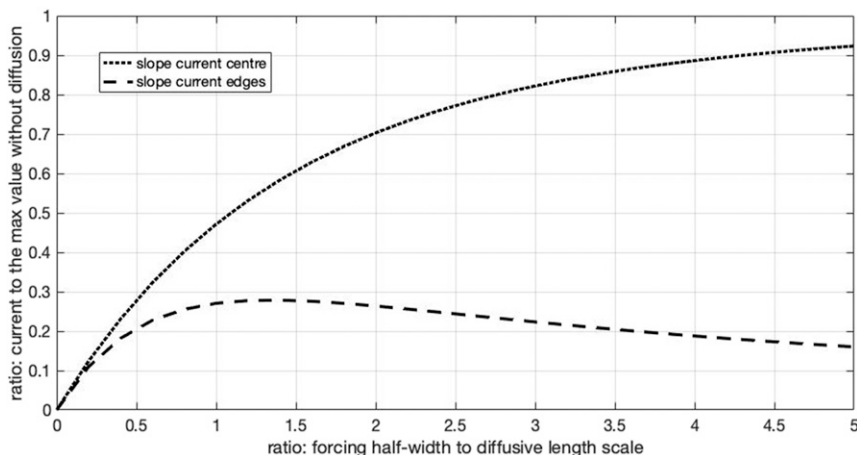
FIG. B1. Illustration of effect of lateral viscosity on forced slope current. The abscissa is the ratio of forcing half-width to diffusive length scale (the effect of diffusion decreases to the right), defined as *a*. The upper curve shows ratio of slope current maximum to the value without diffusion. The lower curve shows the ratio of the current at the edge of the forcing to the maximum value without diffusion (as diffusion increases—to the left—the current becomes almost the same at its maximum and at the edge of the forcing).

Spatial (along slope) variation of the forcing (by upwelling-favorable winds) is considered by Samelson (2017). In this context the response is of course also spatially varying along the slope; the response also includes a baroclinic planetary wave component.

APPENDIX D

Other Forcings

Along-slope flow may result from JEBAR (along-slope pressure gradient) and wind stress as formulated above. Other forcings include freshwater runoff, geostrophic adjustment after mixing, bias in form drag and hence the response to varying wind stress, rectification through nonlinearity of oscillatory motion (e.g., eddies, tidal currents, internal waves). Wind-driven ocean gyres (*y* dependent) include eastern and western ocean boundary currents having widths related to Rossby wave spatial-decay scales. Most of these forcings vary strongly along slope and are hence outside the scope of the present discussion. However, we briefly present two of these.

(i) *Asymmetric form drag.* Flow along the continental slope in the sense opposite to coastal trapped wave propagation is subject to form drag due to bottom "roughness" (Brink 1986; Haidvogel and Brink 1986; Samelson and Allen 1987); drag on flow in the sense of coastal trapped wave propagation is much less. If the form drag is very effective and we

consider a simple case of barotropic flow forced only by an oscillatory along-slope wind stress $\tau_s^y \sin(\sigma t)$ then linearized (1b) becomes

$$\frac{\partial v}{\partial t} - \frac{\tau_s^y}{\rho h}\sin(\sigma t) + rv/h = \frac{\partial v}{\partial t} - \frac{\partial \tau^y}{\rho \partial z} = -g\frac{\partial \eta}{\partial y} = 0$$

by (5) if the forcing is only over the shelf and slope. If $v = 0$ corresponding to large drag r when the flow "would be" in the opposite sense to coastal trapped wave propagation, then the solution is

$$v = \frac{\frac{\tau_s^y}{\rho h}\left[\frac{r}{h}\sin(\sigma t) - \sigma\cos(\sigma t)\right]}{\left[\sigma^2 + \left(\frac{r}{h}\right)^2\right]} \quad [0 < \sigma t < \tan^{-1}(\sigma t)],$$

and $v = 0$ for the remainder of $0 < \sigma t < 2\pi$. For large friction ($r/h\sigma \gg 1$) the mean of v tends to $\tau_s^y/\rho\pi r$. For small friction ($r/h\sigma \ll 1$) the mean of v tends to $1.085\tau_s^y r/(\rho\sigma h^2)$ approximately.

(ii) *Wave, eddy, or tide rectification.* Eddies (for example) may form from instability of the along-slope flow, as exemplified in the California Current system (e.g., Marchesiello et al. 2003). This is especially so in regions of strong upwelling, albeit not the particular focus here. Topographic Rossby waves incident from the ocean may yield their mean onshore flux of longshore momentum to drive alongshore flow (Garrett 1979). Oscillatory flow from wind forcing (Denbo and Allen 1983), or tidal currents (Huthnance 1981), may be rectified to give mean

along-slope flow. The latter give flow of order $h^{-3}(\partial h/\partial x)fQ^2\sigma^2$, where Q is cross-slope fluctuating transport.

REFERENCES

Benthuysen, J., R. Furue, J. P. McCreary, N. L. Bindoff, and H. E. Phillips, 2014: Dynamics of the Leeuwin Current: Part II. Impacts of mixing, friction, and advection on a buoyancy-driven eastern boundary current over a shelf. *Dyn. Atmos. Oceans*, **65**, 39–63, https://doi.org/10.1016/j.dynatmoce.2013.10.004.

Brink, K. H., 1986: Topographic drag due to barotropic flow over the continental shelf and slope. *J. Phys. Oceanogr.*, **16**, 2150–2158, https://doi.org/10.1175/1520-0485(1986)016<2150:TDDTBF>2.0.CO;2.

——, 2016: Cross-shelf exchange. *Annu. Rev. Mar. Sci.*, **8**, 59–78, https://doi.org/10.1146/annurev-marine-010814-015717.

Connolly, T. P., B. M. Hickey, I. Shulman, and R. E. Thomson, 2014: Coastal trapped waves, alongshore pressure gradients, and the California Undercurrent. *J. Phys. Oceanogr.*, **44**, 319–342, https://doi.org/10.1175/JPO-D-13-095.1.

Csanady, G. T., 1978: Arrested topographic wave. *J. Phys. Oceanogr.*, **8**, 47–62, https://doi.org/10.1175/1520-0485(1978)008<0047:TATW>2.0.CO;2.

Denbo, D. W., and J. S. Allen, 1983: Mean flow generation on a continental margin by periodic wind forcing. *J. Phys. Oceanogr.*, **13**, 78–92, https://doi.org/10.1175/1520-0485(1983)013<0078:MFGOAC>2.0.CO;2.

Frouin, R., A. F. G. Fiuza, I. Ambar, and T. J. Boyd, 1990: Observations of a poleward surface current off the coasts of Portugal and Spain during winter. *J. Geophys. Res. Oceans*, **95**, 679–691, https://doi.org/10.1029/JC095iC01p00679.

Furue, R., J. P. McCreary, J. Benthuysen, H. E. Phillips, and N. L. Bindoff, 2013: Dynamics of the Leeuwin Current: Part I. Coastal flows in an inviscid, variable-density, layer model. *Dyn. Atmos. Oceans*, **63**, 24–59, https://doi.org/10.1016/j.dynatmoce.2013.03.003.

Garrett, C. J. R., 1979: Topographic Rossby waves off East Australia; identification and role in shelf circulation. *J. Phys. Oceanogr.*, **9**, 244–253, https://doi.org/10.1175/1520-0485(1979)009<0244:TRWOEA>2.0.CO;2.

Graham, J. A., and Coauthors, 2018: AMM15: A new high-resolution NEMO configuration for operational simulation of the European north-west shelf. *Geosci. Model Dev.*, **11**, 681–696, https://doi.org/10.5194/gmd-11-681-2018.

Guihou, K., J. Polton, J. Harle, S. Wakelin, E. O'Dea, and J. Holt, 2017: Kilometric scale modeling of the North West European shelf seas: Exploring the spatial and temporal variability of internal tides. *J. Geophys. Res. Oceans*, **123**, 688–707, https://doi.org/10.1002/2017JC012960.

Haidvogel, D. B., and K. H. Brink, 1986: Mean currents driven by topographic drag over the continental shelf and slope. *J. Phys. Oceanogr.*, **16**, 2159–2171, https://doi.org/10.1175/1520-0485(1986)016<2159:MCDBTD>2.0.CO;2.

Holliday, N. P., S. A. Cunningham, C. Johnson, S. F. Gary, C. Griffiths, J. F. Read, and T. Sherwin, 2015: Multidecadal variability of potential temperature, salinity, and transport in the eastern subpolar North Atlantic. *J. Geophys. Res. Oceans*, **120**, 5945–5967, https://doi.org/10.1002/2015JC010762.

Huthnance, J. M., 1981: Waves and currents near the continental shelf edge. *Prog. Oceanogr.*, **10**, 193–226, https://doi.org/10.1016/0079-6611(81)90004-5.

——, 1984: Slope currents and "JEBAR." *J. Phys. Oceanogr.*, **14**, 795–810, https://doi.org/10.1175/1520-0485(1984)014<0795:SCA>2.0.CO;2.

——, 1986: The Rockall slope current and shelf-edge processes. *Proc. Roy. Soc. Edinburgh*, **88B**, 83–101, https://doi.org/10.1017/S0269727000004486.

Inall, M. E., T. P. Rippeth, and T. J. Sherwin, 2000: Impact of nonlinear waves on the dissipation of internal tidal energy at a shelf break. *J. Geophys. Res.*, **105**, 8687–8705, https://doi.org/10.1029/1999JC900299.

——, D. Aleynik, T. J. Boyd, M. Palmer, and J. Sharples, 2011: Internal tide coherence and decay over a wide shelf sea. *Geophys. Res. Lett.*, **38**, L23607, https://doi.org/10.1029/2011GL049943.

Lozier, M. S., and Coauthors, 2019: A sea change in our view of overturning in the subpolar North Atlantic. *Science*, **363**, 516–521, https://doi.org/10.1126/science.aau6592.

Marchesiello, P., J. C. McWilliams, and A. Shchepetkin, 2003: Equilibrium structure and dynamics of the California Current System. *J. Phys. Oceanogr.*, **33**, 753–783, https://doi.org/10.1175/1520-0485(2003)33<753:ESADOT>2.0.CO;2.

Marsh, R., I. D. Haigh, S. A. Cunningham, M. E. Inall, M. Porter, and B. I. Moat, 2017: Large-scale forcing of the European Slope Current and associated inflows to the North Sea. *Ocean Sci.*, **13**, 315–335, https://doi.org/10.5194/os-13-315-2017.

Samelson, R. M., 2017: Time-dependent linear theory for the generation of poleward undercurrents on Eastern boundaries. *J. Phys. Oceanogr.*, **47**, 3037–3059, https://doi.org/10.1175/JPO-D-17-0077.1.

——, and J. S. Allen, 1987: Quasi-geostrophic topographically generated mean flow over the continental margin. *J. Phys. Oceanogr.*, **17**, 2043–2064, https://doi.org/10.1175/1520-0485(1987)017<2043:QGTGMF>2.0.CO;2.

Simmons, H. L., S. R. Jayne, L. C. St. Laurent, and A. J. Weaver, 2004: Tidally driven mixing in a numerical model of the ocean general circulation. *Ocean Modell.*, **6**, 245–263, https://doi.org/10.1016/S1463-5003(03)00011-8.

Simpson, J. H., and J. Sharples, 2012: *Introduction to the Physical and Biological Oceanography of Shelf Seas*. Cambridge University Press, 424 pp.

Smith, R. L., A. Huyer, J. S. Godfrey, and J. A. Church, 1991: The Leeuwin Current off Western Australia, 1986-1987. *J. Phys. Oceanogr.*, **21**, 323–345, https://doi.org/10.1175/1520-0485(1991)021<0323:TLCOWA>2.0.CO;2.

Souza, A. J., J. H. Simpson, M. Harikrishnan, and J. Malarkey, 2001: Flow structure and seasonality in the Hebridean slope current. *Oceanol. Acta*, **24**, 63–76, https://doi.org/10.1016/S0399-1784(00)01103-8.

Stashchuk, N., and V. Vlasenko, 2017: Bottom trapped internal waves over the Malin Sea continental slope. *Deep-Sea Res. I*, **119**, 68–80, https://doi.org/10.1016/j.dsr.2016.11.007.

——, ——, P. Hosegood, and W. A. M. Nimmo-Smith, 2017: Tidally induced residual current over the Malin Sea continental slope. *Cont. Shelf Res.*, **139**, 21–34, https://doi.org/10.1016/j.csr.2017.03.010.